Effects of environment on the electron-impact ionization dynamics of argon clusters

Jiaqi Zhou,[1,2] Maomao Gong,[3,4] Oleg Zatsarinny,[5,*] Deepthy Maria Mootheril,[2] Xing Wang,[1] Xiaorui Xue,[1] Shaokui Jia,[1] Jian-Xing Li,[1] Klaus Bartschat,[5] Xiangjun Chen,[3] Alexander Dorn,[2] and Xueguang Ren[1,2,†]

[1]*School of Physics, Xi'an Jiaotong University, Xi'an 710049, China*

[2]*Max-Planck-Institut für Kernphysik, Saupfercheckweg 1, 69117 Heidelberg, Germany*

[3]*Hefei National Research Center for Physical Sciences at the Microscale and Department of Modern Physics, University of Science and Technology of China, Hefei 230026, China*

[4]*School of Physics and Information Technology, Shaanxi Normal University, Xi'an 710119, China*

[5]*Department of Physics and Astronomy, Drake University, Des Moines, Iowa 50311, USA*

(Received 28 September 2022; accepted 16 November 2022; published 12 December 2022)

Ionization of the $3p$ orbital of argon (Ar) monomers, dimers (Ar_2), and small-size Ar clusters (Ar_n, $\langle n \rangle \approx 15$) is investigated for 90-eV electron impact. Experimentally, the three-dimensional momentum vectors of the two outgoing electrons and the residual ion are measured in triple coincidence, as is the mass-over-charge ratio of the ion, using a reaction microscope that covers a large part of the final-state phase space. The triple-differential cross sections (TDCS) are obtained for almost the full solid angle of the ejected electron, in which the data for Ar monomers are well reproduced by B-spline R-matrix calculations for ejected electron energies of 3 eV, 5 eV, and 10 eV, and projectile scattering angles of 10° and 20°. Compared to the Ar monomer, the cross sections for Ar_2 and Ar_n exhibit effects due to the neighboring atoms by the suppression of binary and recoil lobes and the enhanced electron emission out of the projectile scattering plane. These environmental effects are further investigated using a multicenter three-distorted-wave theory, which can generate the TDCSs for electron-impact ionization of Ar_2. These studies reveal an important role of multicenter scattering reactions on the ionization dynamics of Ar clusters. Moreover, a two-center interference is not found in the TDCS of Ar_2. This is interpreted as due to the involvement of orbitals with both gerade and ungerade symmetries in the ionization process.

DOI: 10.1103/PhysRevA.106.062811

I. INTRODUCTION

Electron-impact ionization of atoms and molecules plays a fundamental role in a range of basic science and practical applications, such as modeling electron radiation processes in planetary atmospheres, optimization of energy transfer in reactive plasmas, and understanding radiation damage in biological tissues [1–5]. One way of comprehensively characterizing the ionization reaction is to perform kinematically complete (e, 2e) experiments, in which the linear momentum vectors of all final-state particles are determined. The quantity measured in such experiments is the triple-differential cross section (TDCS) [6,7].

In recent years, experimental techniques were developed that allow to study the ionization dynamics over a large fraction of the entire solid angle and a large range of energies of the continuum electrons in the final state [8–10], including measurements of absolute TDCSs [11]. These experiments serve as a powerful tool for comprehensively testing theoretical models that account for the quantum-mechanical few-body interactions.

On the other hand, theory has also made tremendous progress; for simple systems the measured TDCS can be well reproduced by state-of-the-art nonperturbative theories over the full phase space in the final state [12–19]. Sophisticated perturbative methods can also give detailed insight into the relevant interactions and mechanisms. They are more tractable and can be applied to larger systems including biomolecules; see, e.g., Refs. [20–28].

In more complex systems like clusters, where atoms and molecules are embedded in a chemical environment, the ionization mechanisms and dynamics can be affected by adjacent neighbors [29–33]. For example, multiple-scattering reactions are observed in the ionization of Ar clusters, where the cross sections exhibit a modified binary-peak shape as well as a filling of the minimum separating the binary from the recoil lobe [32]. In these studies, however, the experimental data were integrated over a broad range of scattering angles and ejected energies, which can wash out some key features in the ionization cross sections. Additionally, no theoretical calculations obtaining TDCS were available for clusters. Thus, the understanding of the ionization dynamics of clusters remains very incomplete, and hence should be further investigated both experimentally and theoretically. In contrast, theoretical

*Deceased
†renxueguang@xjtu.edu.cn

calculations for elastic scattering on Ar clusters exist and have obtained significant cross-section modifications with respect to monomers [34].

In the present work, we perform a combined experimental and theoretical study of electron-impact ionization dynamics of Ar clusters at 90-eV incident projectile energy. The TDCSs for the Ar monomer, dimer, and small-size clusters (Ar_n, $\langle n\rangle \approx 15$) were measured simultaneously using a multiparticle coincidence momentum spectrometer [8], in which a photoemission electron source was developed to improve the experimental resolution compared to our earlier studies with a thermal-emission cathode [32,35]. Here, ionization of the $3p$ orbital in Ar is considered with possibly additional elastic scattering from the neighboring Ar atoms in the clusters. The measurements cover nearly the entire 4π solid angle for the secondary electron emission energies ranging from 3 eV to 10 eV and projectile scattering angles ranging from 10° to 20°. The experimental TDCSs are internormalized across all measured scattering angles and ejected energies.

The data for the Ar monomer are compared with predictions from *B*-spline *R*-matrix (BSR) calculations. Furthermore, multicenter three-distorted-wave (MCTDW) calculations are carried out to study the influences of the environment on the multicenter scattering effects in the ionization of clusters, where the possibility of electron scattering is calculated by evaluating the transition matrix T in the multicenter potential of an Ar dimer [28]. In addition, we consider the two-center interference effects for the ionization dynamics of Ar_2 [36–40].

This manuscript is organized as follows. We start with a brief description of the experimental method in Sec. II and the theoretical approaches in Sec. III. More details can be found in the references provided. We then present and discuss our results in Sec. IV and finish with our conclusions in Sec. V.

II. EXPERIMENTAL METHOD

The experiment was performed using a reaction microscope, which was particularly designed for electron collision experiments. Since the details about the experimental setup have been given elsewhere [8,35], only a brief description is provided here.

The well-focused pulsed electron beam (∼1 mm diameter) crosses a supersonic cold gas jet, which contains about 2% dimers and 0.6% heavier clusters with a mean cluster size of $\langle n\rangle \approx 15$ [32,41] formed by a 30-μm nozzle, and a two-stage differential pumping system. The pulsed projectile beam is generated from an electron gun in which a tantalum photocathode is irradiated by a pulsed ultraviolet laser beam. The wavelength, repetition rate, and pulse width of the laser beam are 266 nm, 40 kHz, and 0.5 ns, respectively.

In our experiments, the two outgoing electrons and one residual ion are detected in triple coincidence. They are extracted from the target region by means of uniform electric and magnetic fields to opposite directions and projected onto two position- and time-sensitive microchannel plate detectors with hexagonal delay-line position readout. The detection solid angle for the residual ions is 4π, and the acceptance angle for detection of electrons up to an energy of 15 eV is also close to 4π, except for the acceptance holes at small forward and backward angles where the electrons end up in a detector bore, which is required to dump the primary beam. For each detected particle, the three-dimensional momentum vector is reconstructed from the time-of-flight (TOF) and the position of impact on the detector.

III. THEORETICAL MODELS

We compare the experimental TDCS of Ar monomers with theoretical prediction from the BSR approach. In addition, we obtained the TDCSs for both Ar_2 and Ar to study the effects of the environment on the ionization dynamics of Ar clusters using the currently available MCTDW approach (MCTDW-Mee). The latter includes a final-state Coulomb distortion factor Mee from the repulsion of the two continuum electrons, often referred to as the postcollision interaction (PCI) effect, which is approximated by the Gamow factor calculated with the Ward-Macek method [42]:

$$\left|C_{12}^{\mathrm{WM}}\right|^2 = N_{ee}\left|1F_1\left(i\gamma,\,1,\,-2ik_{12}r_{12}^{\mathrm{ave}}\right)\right|^2 \tag{1}$$

where r_{12}^{ave} is the average separation of the two outgoing electrons,

$$r_{12}^{\mathrm{ave}} = \frac{\pi^2}{16\epsilon_t}\left(1+\frac{0.627}{\pi}\sqrt{\epsilon_t}\ln\epsilon_t\right)^2, \tag{2}$$

where ϵ_t is the total energy of the two outgoing electrons. N_{ee} is calculated as

$$N_{ee} = \left|e^{-\frac{\pi\gamma}{2}}\Gamma(1-i\gamma)\right|^2 = \frac{\pi/k_{12}}{e^{\pi/k_{12}}-1}, \tag{3}$$

where $\Gamma(1-i\gamma)$ is the gamma function, $k_{12}=\mu v_{12}$, $\mu=1/2$ is the reduced mass for the two electrons, v_{12} is the relative velocity between the two electrons, and $\gamma = 1/v_{12}$ is the Sommerfeld parameter.

The details of the theoretical approaches have already been discussed in Refs. [43,44] for BSR and Refs. [28,45] for MCTDW. The former includes a large number of pseudostates in the close-coupling expansion, which makes it possible to extract the ionization amplitudes and subsequently the cross sections via a projection technique [16]. In the MCTDW-Mee approach, the continuum electrons are described by distorted waves obtained from solving the effective Schrödinger equation,

$$\left[-\tfrac{1}{2}\nabla^2 + V^m - E\right]\mathcal{F}^{(-)} = 0, \tag{4}$$

where E is the energy of continuum electron and V^m is the adopted model potential,

$$V^m = V^{st} + V^{cp} + V^{\text{model exc}}, \tag{5}$$

among which V^{st} is the electrostatic potential and V^{cp} and $V^{\text{model exc}}$ are the correlation-polarization potential and the model exchange potential, respectively. $\mathcal{F}^{(-)}$ is the multicenter continuum wave function solved in the model potential without channel coupling.

IV. RESULTS AND DISCUSSION

In this work, the different product species Ar^+, Ar_2^+, and Ar_n^+ are distinguished by the measured mass-over-charge

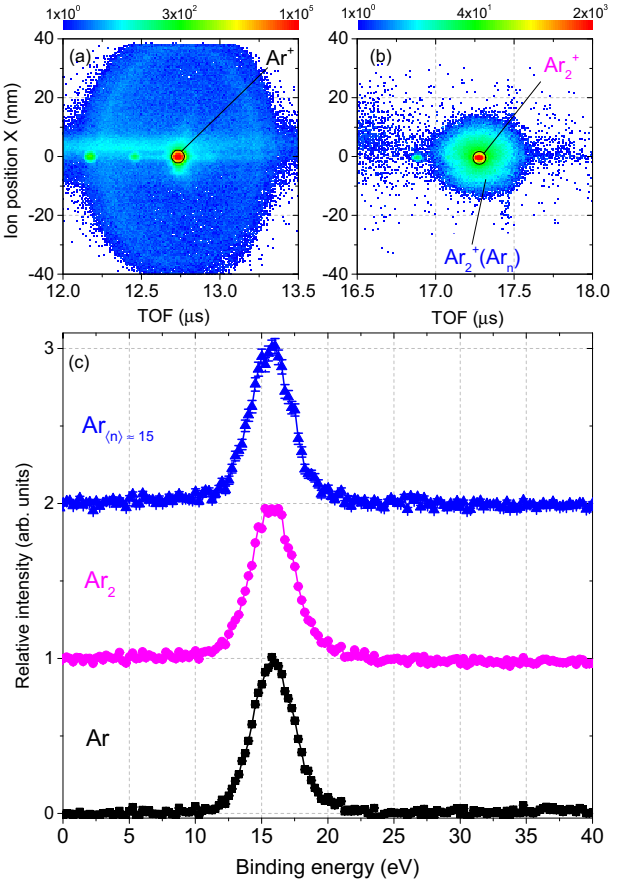

FIG. 1. Position coordinate x vs TOF of (a) Ar^+ and (b) $Ar_2{}^+$ and $Ar_n{}^+$ ions. (c) Binding energy spectra for the ionization of Ar monomers, Ar_2 dimers, and small-size argon clusters (Ar_n, $\langle n\rangle \approx 15$). The spectra are offset along the vertical axis and each normalized to unity at their respective maximum.

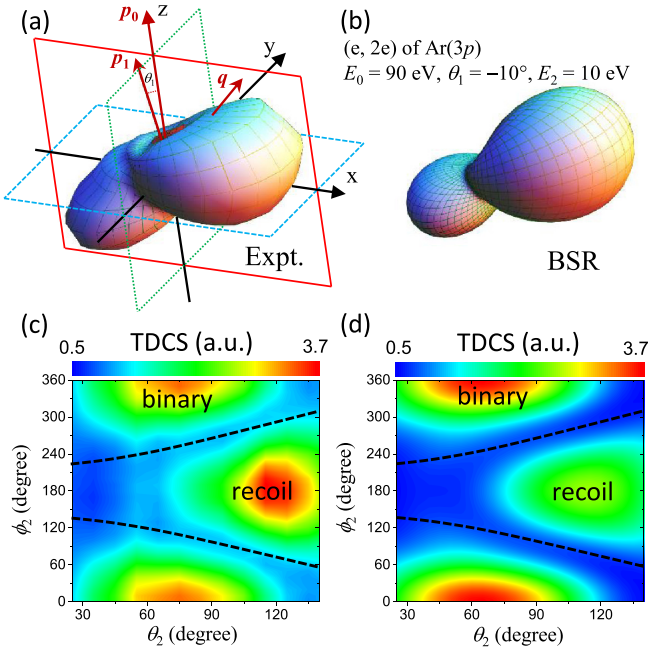

FIG. 2. Experimental and theoretical TDCSs for ionization of Ar($3p$) by incident electrons with energy $E_0 = 90$ eV, presented as 3D images. The scattering angle of the projectile is $\theta_1 = -10^\circ$ and the ejected electron energy is $E_2 = 10$ eV. (a) and (c): Experimental TDCS; (b) and (d): BSR predictions.

spectrum and the ion momenta. In Figs. 1(a) and 1(b) the ion intensity as a function of TOF and one transversal position on the ion detector (x coordinate) is shown. The sharp spots labeled by circles correspond to ions with small initial momentum and are attributed to Ar^+ and $Ar_2{}^+$ from ionization of Ar monomers and dimers, respectively. Diffuse intensity circles centered around the sharp spots correspond to larger ion momenta and indicate a dissociative process following ionization. In Fig. 1(a), the diffuse distribution around the central spot corresponds to fast Ar^+ ions mainly due to the Coulomb explosion of Ar dimers [46,47] and due to dissociation of singly ionized dimers (see below). The diffuse intensity in Fig. 1(b) is assigned to the ionization of Ar clusters, which subsequently fragment into $Ar_2{}^+$ and neutral species [$Ar_n{}^+ \rightarrow Ar_2{}^+ + (n\text{-}2)$ Ar]. The ions were detected in coincidence with the two outgoing electrons. As shown in Fig. 1(c), we can obtain the binding energy spectra for ionization of the different target species. The binding energy is defined as the incident projectile energy minus the summed energy of the two outgoing electrons, i.e., $E_{\rm bind} = E_0 - (E_1 + E_2)$. For all species, one can see a single peak centered at around 15.8 eV, which corresponds to single ionization of the outer $3p$ electron of Ar. From these spectra, we determine a binding energy resolution of about 3.6 eV (full width at half maximum) for the present measurements, which turns out to be a factor of ~3 better than our previous results [32]. Additionally, the spectrum for Ar shows weak structures at around 35–40 eV, which are attributed to the population of satellite states $Ar^{+*}(3p^{-2}nl)$ [47,48]. For Ar dimers and clusters, there might be additional elastic and inelastic scattering reactions at the neighboring Ar atom(s). For Ar clusters, we observe a rather small inelastic scattering peak at $E_{\rm bind} \approx 27$ eV which is much smaller compared to the results of Ref. [32]. This is because we obtained a smaller mean cluster size in the present work, leading to the reduced possibility of multiple scattering reactions.

Figure 2 shows the experimental and theoretical TDCSs for 90-eV electron-impact ionization of atomic Ar($3p$) as three-dimensional (3D) polar plots. The projectile scattering angle and ejected electron energy are fixed to $\theta_1 = -10^\circ$ and $E_2 = 10$ eV, respectively. The left panel is derived from the experimental data, while the right panel corresponds to the calculated result from the BSR model. In these representations the projectile ($\boldsymbol{p_0}$) enters from the bottom and is scattered ($\boldsymbol{p_1}$) to the left (hence the minus in the notation for the scattering angle θ_1). These two momentum vectors define the scattering (xz) plane as indicated by the solid frame in Fig. 2(a). The momentum transfer to the target is indicated by the arrow labeled $\boldsymbol{q}$. The (relative) TDCS for a particular direction is given as the distance from the origin of the plot to the point on the surface, which is intersected by the ionized electron's emission angle (θ_2, ϕ_2). In addition, Figs. 2(c) and 2(d) present the two-dimensional (2D) maps of experimental and theoretical TDCSs as a function of polar angle θ_2 (with respect to the z axis) and azimuth angle ϕ_2 (with respect to the x axis) of the emitted electron direction, respectively. The binary and

recoil lobes which originate from a single projectile collision within the target are observable as the islands with maximum intensity in the 2D maps, which lie in the scattering plane. Collisions where the projectile undergoes more than one scattering process within a monomer/cluster (e.g., high-order projectile-ion or projectile-ejected electron interactions in the monomer [49,50] and scattering with additional atoms in the cluster [32]) could result in a more isotropic electron emission and enhance the low cross section in between the binary and recoil lobes. These regions are indicated by the dashed curves, and the intensity there is referred to as out-of-plane structures in the following discussion.

The typical two-lobe structure for the electron emission pattern of Ar [6,7,50,51] consists of the binary lobe, which is roughly along the direction of the momentum transfer $\boldsymbol{q}$, thus corresponding to electrons carrying the momentum transferred by the projectile. The recoil lobe is found in the opposite direction, where the outgoing electron, initially moving in the binary direction, backscatters in the ionic potential. Additionally, the ejected electron is repelled by the scattered projectile due to the long-range nature of the Coulomb force. This PCI tilts the binary and recoil lobes away from the scattered projectile direction. Comparing the experimental with the calculated data, we see that the BSR results are in overall good agreement with the measured data, except for the relatively smaller magnitude of the recoil lobe. The 3D cross section presented in the present work is consistent with our previous results of Ar($3p$) ionization at impact energies from 66 eV to 195 eV [10,52–54], and the good agreements between experiment and calculation confirm that the BSR model is quite reliable to predict the cross section of electron impact ionization of Ar monomers.

For a more quantitative comparison between experiment and theory, the cross sections in three orthogonal planes are presented in Fig. 3. These are cuts through the 3D TDCS image, as indicated in Fig. 2(a) by the solid, dashed, and dotted frames, corresponding to the xz scattering plane, the yz half-perpendicular plane, and the xy full-perpendicular plane. These planes are shown in the left, middle, and right columns of the figure, respectively. The kinematical conditions studied in this work are the projectile scattering angles of $\theta_1 = -10^\circ$ and -20°, and ejected-electron energies of $E_2 = 3.0$ eV, 5.0 eV, and 10.0 eV. A single, global scaling factor used to normalize the experimental data was found by achieving a good visual fit between the experiment and the BSR predictions for the TDCS in the scattering plane at $\theta_1 = -10^\circ$ and $E_2 = 10.0$ eV; see Fig. 3(c). This factor was subsequently applied to all other kinematics and planes, i.e., the experimental data remain consistently cross-normalized to each other.

As shown in Fig. 3 for the scattering plane (i.e., the xz plane), the BSR prediction is in rather good agreement with the experimental data. For the low ejected electron energies ($E_2 = 3$ eV, 5 eV), the binary peak exhibits a double-peak structure with a minimum near the momentum transfer direction. This is the result of the characteristic momentum profile of a p orbital that has a node for vanishing momentum. For larger E_2, the double binary peaks tend to merge into a single peak. For the recoil lobes, the experiments show a main peak located at θ_2 between about 240° and 270°, followed by a small shoulder near 300°.

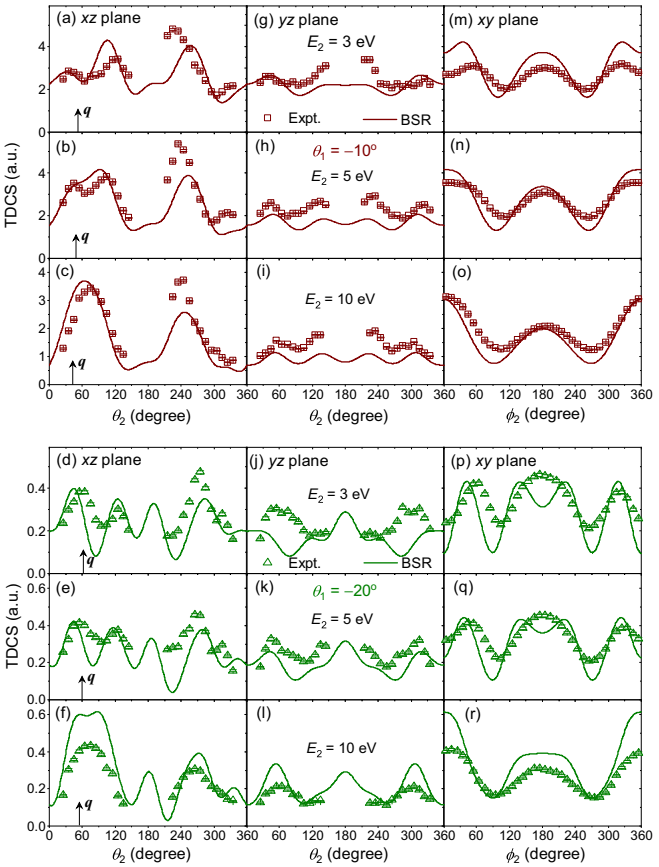

FIG. 3. Experimental (squares and triangles) and theoretical (solid line) TDCSs for ionization of Ar($3p$) as a function of the ejected-electron emission angle at scattering angles $\theta_1 = -10^\circ$ (top nine panels) and -20° (bottom nine panels) for ejected-electron energies $E_2 = 3.0$ eV, 5.0 eV, and 10.0 eV, respectively. Starting from the left column are TDCSs in the xz (scattering), yz (half-perpendicular), and xy (full-perpendicular) planes.

The measured cross sections in the scattering plane are well reproduced by the BSR calculations, except for the predicted lower intensity in the recoil lobes. In addition, the BSR model shows a peak at θ_2 close to 180° which is particularly strong for the case of $\theta_1 = -20^\circ$. Experimentally the cross section in this region is not accessible due to the central beam dump in the electron detector so that electrons emitted forwards or backwards are not detected.

For the half-perpendicular plane (i.e., the yz plane), symmetry considerations require the cross sections to be identical above and below the scattering plane, and therefore, in the diagrams it is symmetric with respect to 180°. The experimental data show maxima at θ_2 around 60° and 300° originating from the binary peak, while the recoil lobe gives rise to the central pattern at θ_2 near 180°. There is overall good qualitative agreement between the BSR predictions and the experimental data concerning both the angular dependence of the cross sections and the relative magnitude over the entire angular range and for the energies analyzed. Noticeable deviations occur for $\theta_1 = -20^\circ$ and $E_2 = 3$ eV, where the experiment shows maxima at $\theta_2 \approx 60^\circ$ and 300°, while two symmetric minima are obtained in the BSR calculations. Furthermore,

the BSR theory predicts a lower intensity for the central peak than found experimentally, in particular for $\theta_1 = -10^\circ$. The BSR results show a maximum at $\theta_2 = 180^\circ$ for $\theta_1 = -10^\circ$ but a small dip for $\theta_1 = -20^\circ$. Unfortunately, the cross section in this region cannot be accessed in our experiment.

For the full-perpendicular plane (i.e., the xy plane), the experimental angular acceptance covers the entire angular range ($0^\circ - 360^\circ$), and the cross sections are again symmetric with respect to 180°. The peaks in the vicinity of $\phi_2 = 0^\circ$ and 180° correspond to the binary and recoil peaks, respectively. The BSR theory is in rather good agreement with the experimental data, except for the predicted dips at $\phi_2 = 180^\circ$ for $\theta_1 = -20^\circ$ and $E_2 = 3$ eV and 5 eV, which are shown in Figs. 3(p) and 3(q), respectively.

In the following we investigate the environment effects on the ionization dynamics of Ar clusters by comparing the results of Ar monomers, dimers, and small-size clusters, which were simultaneously measured in the experiment. The TDCSs in 3D images for Ar_2 and Ar_n, ($\langle n \rangle \approx 15$) are presented in Figs. 4(a) and 4(b), respectively, at $\theta_1 = -10^\circ$ and an ejected-electron energy of $E_2 = 10$ eV. While the basic binary and recoil lobes are maintained, these 3D plots exhibit an enhancement of the out-of-plane cross sections, in particular for the Ar_n clusters.

For more quantitative studies, we present the TDCS ratios between clusters and monomers for $\sigma(Ar_2)/\sigma(Ar)$ and $\sigma(Ar_n)/\sigma(Ar)$ in Figs. 4(c) and 4(d), respectively. Here, the cross sections are scaled according to the measured total yields of Ar^+, $Ar_2{}^+$, and $Ar_2{}^+(Ar_n)$ ions (Fig. 1). In the cross-section ratios the binary (dotted ellipse) and recoil (solid ellipse) lobes are suppressed in comparison with Ar monomers, while the out-of-plane cross section (dashed curves) is enhanced. This can originate from multicenter scattering effects [32,49,50], i.e., the electron emission angles can be redistributed due to additional elastic scattering from the neighbors, with an increasing rescattering probability expected in clusters.

In addition, the cross sections in three orthogonal (xz, yz, and xy) planes are presented in Fig. 4(e) for the ionization of Ar monomer, Ar_2 dimer, and larger Ar_n clusters. These comparisons show similar features as the results in Figs. 4(c) and 4(d), where the cluster effects are observed more clearly, in particular for the case of Ar_n. For the xz scattering plane, the binary and recoil lobes in Ar_2 show a small decrease with respect to Ar monomer, and more suppression is observed for the case of larger Ar_n clusters. The decrease of the binary peak is also visible in the xy full-perpendicular plane at ϕ_2 around 0° and 360°. Here, the minima around $\phi_2 = 90^\circ$ and 270°, which separate the binary from the recoil lobes, are filled due to the enhanced electron emission out of the scattering plane. While an overall enhancement is observed in the yz half-perpendicular plane, especially for the TDCS of larger Ar_n clusters, in this plane the cross sections are less affected by the binary and recoil lobes and thus more sensitive to such higher-order effects [32,49,50].

To obtain more insight into the environment effects, calculations of the TDCS for Ar_2 are performed using the MCTDW method. According to the theoretical potential-energy curves of $Ar_2{}^+$ [55,56], the ionic $(3p\sigma_g)^{-1}$ and $(3p\pi_u)^{-1}$ states of the dimer can dissociate into $Ar^+ + Ar$ species, and the ionization

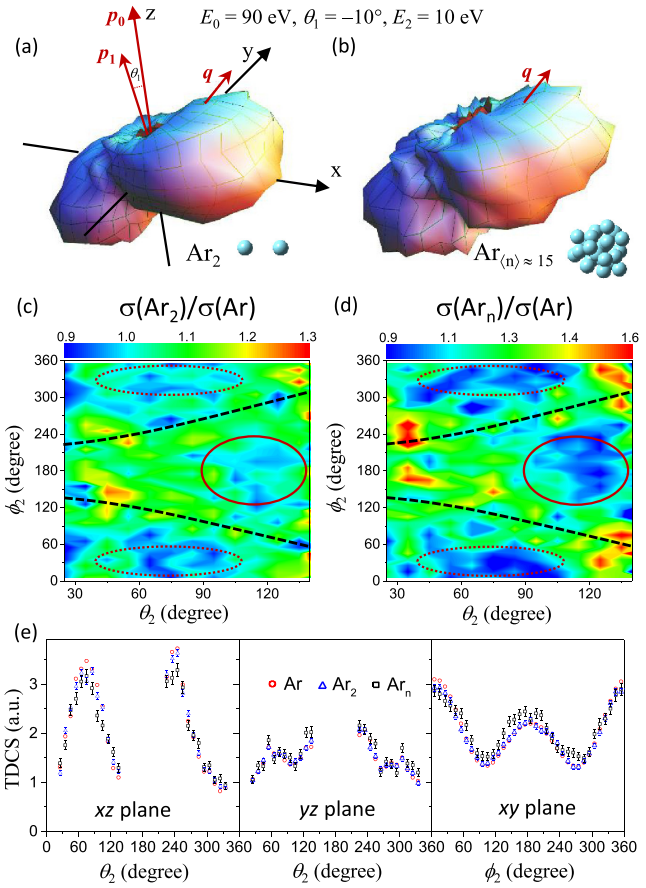

FIG. 4. Experimental TDCSs for ionization of (a) Ar_2 and (b) Ar_n, ($\langle n \rangle \approx 15$) by incident electrons with energy $E_0 = 90$ eV, presented as 3D images. The scattering angle of the projectile is $\theta_1 = -10^\circ$ and the ejected electron energy is $E_2 = 10$ eV. Two-dimensional map of the cross-sectional ratios for (c) $\sigma(Ar_2)/\sigma(Ar)$ and (d) $\sigma(Ar_n)/\sigma(Ar)$. The dashed curves correspond to the connection of the binary and recoil lobes, i.e., the out-of-plane cross section. The dotted and solid ellipses denote the binary and recoil lobes, respectively. (e) Experimental TDCSs for ionization of Ar (circles), Ar_2 (triangles), and Ar_n (squares) as a function of the ejected-electron emission angle in the scattering (xz), perpendicular (yz), and full-perpendicular (xy) planes.

of $3p\sigma_u$ and $3p\pi_g$ orbitals in Ar_2 can lead to stable $Ar_2{}^+$ ions. Considering spin-orbit coupling, the situation becomes complicated and the removal of an electron from $3p\sigma_u$, $3p\pi_g$, and $3p\pi_u$ can contribute to the bound ionic states of the Ar_2 dimers [55,57]. Since experimentally we identify collisions with dimers via a coincidence with $Ar_2{}^+$, we consider ionization of these three orbitals for calculating the TDCS of Ar_2, i.e., $\sigma(Ar_2)$. Here, the wave functions of the bound orbitals of Ar_2 are calculated using the GAUSSIAN 16 program [58] by the density functional theory method employing the B3LYP hybrid functional with aug-cc-pVTZ basis set. The Ar_2 ionization of different orbitals is considered as an incoherent process due to the populations of different ionic final states. Thus the calculated TDCSs for different orbitals are summed incoherently as $\sigma(3p\sigma_u) + 2 \times \sigma(3p\pi_g) + 2 \times \sigma(3p\pi_u)$, where the relative statistical weights are obtained considering the orbital degeneracy.

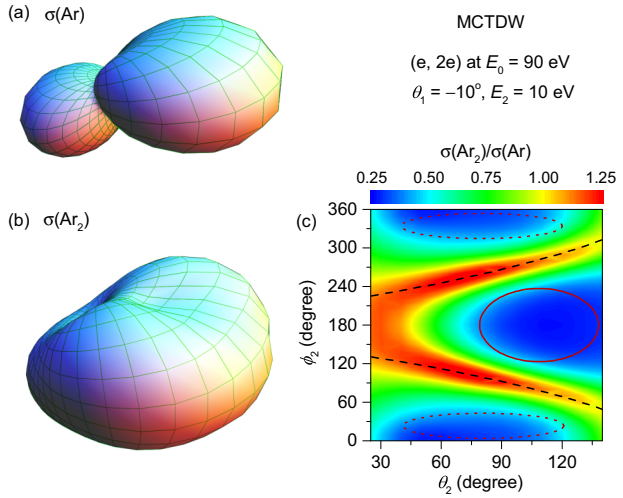

FIG. 5. Calculated TDCSs using MCTDW for the $3p$-orbital ionization of (a) Ar monomer and (b) Ar_2 dimer with incident electron energy $E_0 = 90$ eV, presented as 3D images. The scattering angle of the projectile is $\theta_1 = -10^\circ$ and the ejected-electron energy is $E_2 = 10$ eV. (c) Two-dimensional plot of cross-sectional ratios for Ar_2^+ and Ar^+.

The calculated 3D TDCS for Ar monomer using the MCTDW method is presented in Fig. 5(a), which is in generally good agreement with the experimental data and also the prediction from the BSR theory shown in Figs. 2(a) and 2(b), respectively, while the calculated result for the Ar_2 dimer, shown in Fig. 5(b), exhibits a strong enhancement of the out-of-plane cross sections in comparison with the results of Ar monomer. Additionally, we present the TDCS ratio between $\sigma(Ar_2)$ and $\sigma(Ar)$ in Fig. 5(c), where the predicted features, i.e., the suppression of the binary (dotted ellipse) and recoil (solid ellipse) lobes and the enhancement of the out-of-plane structures (dashed curves), are in reasonable qualitative agreement with the experimental results. These results emphasize the importance of the environment effect in electron-impact ionization of clusters. We also notice that in the calculation both suppression and enhancement are stronger than in the experimental data. The underlying reason may be an overestimation of the multicenter scattering potential in the dimers. Here, after ionization of Ar_2 the single charge is more likely localized at one Ar atom due to the large interatomic distance of the dimer, while in our calculation the single charge is considered to be shared by both Ar atoms like the ionization of a diatomic molecule, and therefore the model can overestimate the effect of the neighboring atom. Future studies are expected for considerations of a localized state in the ionization process, e.g., by coherently superimposing the $3p\pi_g$ and $3p\pi_u$ or $3p\sigma_g$ and $3p\sigma_u$ orbitals.

Finally, following Stia *et al.* [36], we consider ionization of the dimer formally as the coherent electron emission from two neighboring atoms. This can be described as a two-center interference, which is schematically shown in Fig. 6(a). In this description an electron emission angle–dependent interference can be expected, since the de Broglie wavelength of a 10-eV electron (3.88 Å) and the interatomic distance of Ar_2 (3.8 Å) are nearly identical in size [36–40]. According to

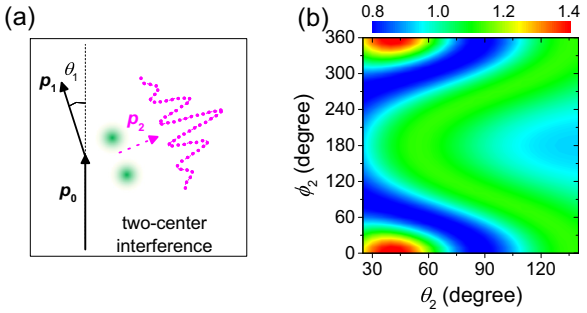

FIG. 6. (a) Schematic diagram for the collision kinematics of two-center interference. (b) Calculated interference factor for the average molecular orientation within the 4π solid angle, plotted as a function of the emission angles θ_2 and ϕ_2 of the ejected electrons.

theory [36], the TDCS for a two-center system like Ar_2 with random spatial alignment can be determined as the TDCS for the corresponding Ar atom multiplied by an interference factor:

$$\sigma(Ar_2) = 2\sigma(Ar)\left(1 + \frac{\sin(\boldsymbol{\chi}\cdot\boldsymbol{R})}{\boldsymbol{\chi}\cdot\boldsymbol{R}}\right) \tag{6}$$

Here $\boldsymbol{R}$ is the interatomic distance and $\boldsymbol{\chi}$ is the momentum transferred to the residual ion.

The two-center interference pattern can be obtained by the cross-section ratio between $\sigma(Ar_2)$ and $\sigma(Ar)$, which is shown in Fig. 6(b). This spectrum exhibits maxima in the binary region, which is in sharp contrast to the experimental data depicted in Fig. 4(c) and the MCTDW calculation shown in Fig. 5(c). This shows that the description of dimer ionization by the interference model which originally was derived for the hydrogen molecule is not adequate. This model does not account for molecular effects such as the dissociative nature of molecular states in Ar_2, where the atomic orbitals involved do not contribute to the measured ionization signal. Furthermore, the model was developed for the ground state of H_2 consisting of a gerade combination of atomic orbitals. The present results originate from the ionization of $3p\sigma_u$, $3p\pi_g$, and $3p\pi_u$ orbitals. These orbitals consist of atomic states that are either in phase ($3p\sigma_u$, $3p\pi_u$) or out of phase ($3p\pi_g$). Therefore, there is a phase difference of π between both interference patterns such that the fringes might be washed away in the summed intensity. Furthermore, there are also other effects that can influence the simple two-center interference factor. For example, according to high-energy (e, 2e) electron momentum spectroscopy studies of CF_4, there might be an additional higher-order term in the interference model [59]. Studies on the ionization dynamics of the aligned H_2 molecule have revealed that the molecular potential in the final state can modify the two-center interference pattern and cause electron emission preferentially along the molecular axis, in particular for the low ejected energy of $E_2 = 10$ eV [38,60].

V. CONCLUSIONS

In summary, we have studied experimentally and theoretically the effects of the environment on the ionization dynamics of Ar clusters initiated by electron impact at $E_0 =$ 90 eV. We have obtained the triple-differential cross sections

for the Ar monomer, dimer (Ar_2), and small-size Ar clusters (Ar_n, $\langle n \rangle \approx 15$) in three-dimensional kinematics. The BSR calculations show overall good agreement with the cross sections for the Ar monomer for scattering angles $\theta_1 = 10^\circ$ and 20° and ejected energies E_2 of 3 eV, 5 eV, and 10 eV.

In addition to standard binary and recoil lobes, the experimental cross sections for Ar clusters reveal noticeable structures in the out-of-plane region. We also observed the suppression of the binary and recoil lobes for Ar clusters when compared to the results for Ar monomers.

Furthermore, we obtained theoretical cross sections for Ar_2 using the MCTDW method, which considers the influences of the environment on the multicenter scattering effects. The calculations show qualitative agreement with the results for Ar clusters, in particular regarding the suppression of the binary and recoil lobes and the enhancement of the out-of-plane structures. Finally, no two-center interference effect on the electron-impact ionization dynamics of Ar_2 was observed, since orbitals with both gerade and ungerade symmetries are ionized in the present experiments.

Our studies highlight the importance of environment effects in the ionization of clusters, on particular for multicenter scattering reactions. We hope that the results obtained in the present work will also help to interpret the electron-impact ionization process in more complex systems.

ACKNOWLEDGMENTS

This work was supported by the National Natural Science Foundation of China under Grants No. 11974272 and No. 11774281, by the Deutsche Forschungsgemeinschaft under Project No. RE 2966/5-1, and by the NSF under Grants No. OAC-1834740 and No. PHY-2110023 and the XSEDE supercomputer allocation TG-PHY-090031. X.R. is grateful for support from the Open Fund of the State Key Laboratory of High Field Laser Physics (Shanghai Institute of Optics and Fine Mechanics). J.Z. is grateful for support from the China Scholarship Council (CSC).

[1] K. Bartschat and M. J. Kushner, Electron collisions with atoms, ions, molecules, and surfaces: Fundamental science empowering advances in technology, Proc. Natl. Acad. Sci. **113**, 7026 (2016).

[2] E. Alizadeh, T. M. Orlando, and L. Sanche, Biomolecular damage induced by ionizing radiation: The direct and indirect effects of low-energy electrons on DNA, Annu. Rev. Phys. Chem. **66**, 379 (2015).

[3] I. Bray, D. V. Fursa, A. Kadyrov, A. Stelbovics, A. Kheifets, and A. Mukhamedzhanov, Electron- and photon-impact atomic ionisation, Phys. Rep. **520**, 135 (2012).

[4] L. Campbell and M. J. Brunger, Electron collisions in atmospheres, Int. Rev. Phys. Chem. **35**, 297 (2016).

[5] B. C. Garrett, D. A. Dixon, D. M. Camaioni, D. M. Chipman, M. A. Johnson, C. D. Jonah, G. A. Kimmel, J. H. Miller, T. N. Rescigno, P. J. Rossky, S. S. Xantheas, S. D. Colson, A. H. Laufer, D. Ray, P. F. Barbara, D. M. Bartels, K. H. Becker, K. H. Bowen, S. E. Bradforth, I. Carmichael *et al.*, Role of water in electron-initiated processes and radical chemistry: Issues and scientific advances, Chem. Rev. **105**, 355 (2005).

[6] H. Ehrhardt, K. Jung, G. Knoth, and P. Schlemmer, Differential cross sections of direct single electron impact ionization, Z. Phys. D **1**, 3 (1986).

[7] A. Lahmam-Bennani, Recent developments and new trends in (e,2e) and (e,3e) studies, J. Phys. B: At. Mol. Opt. Phys. **24**, 2401 (1991).

[8] J. Ullrich, R. Moshammer, A. Dorn, R. Dörner, L. P. H. Schmidt, and H. Schmidt-Böcking, Recoil-ion and electron momentum spectroscopy: Reaction-microscopes, Rep. Prog. Phys. **66**, 1463 (2003).

[9] M. Dürr, C. Dimopoulou, A. Dorn, B. Najjari, I. Bray, D. V. Fursa, Z. Chen, D. H. Madison, K. Bartschat, and J. Ullrich, Single ionization of helium by 102 eV electron impact: Three-dimensional images for electron emission, J. Phys. B: At. Mol. Opt. Phys. **39**, 4097 (2006).

[10] X. Ren, S. Amami, O. Zatsarinny, T. Pflüger, M. Weyland, A. Dorn, D. Madison, and K. Bartschat, Kinematically complete study of low-energy electron-impact ionization of argon: Internormalized cross sections in three-dimensional kinematics, Phys. Rev. A **93**, 062704 (2016).

[11] J. Zhou, E. Ali, M. Gong, S. Jia, Y. Li, Y. Wang, Z. Zhang, X. Xue, D. V. Fursa, I. Bray, X. Chen, D. Madison, A. Dorn, and X. Ren, Absolute triple differential cross sections for low-energy electron impact ionization of biochemically relevant systems: Water, tetrahydrofuran, and hydrated tetrahydrofuran, Phys. Rev. A **104**, 012817 (2021).

[12] T. N. Rescigno, M. Baertschy, W. A. Isaacs, and C. W. McCurdy, Collisional breakup in a quantum system of three charged particles, Science **286**, 2474 (1999).

[13] I. Bray, Close-Coupling Approach to Coulomb Three-Body Problems, Phys. Rev. Lett. **89**, 273201 (2002).

[14] J. Colgan, M. S. Pindzola, G. Childers, and M. A. Khakoo, Low-energy electron-impact single ionization of helium, Phys. Rev. A **73**, 042710 (2006).

[15] X. Ren, A. Senftleben, T. Pflüger, K. Bartschat, O. Zatsarinny, J. Berakdar, J. Colgan, M. S. Pindzola, I. Bray, D. V. Fursa, and A. Dorn, Propensity for distinguishing two free electrons with equal energies in electron-impact ionization of helium, Phys. Rev. A **92**, 052707 (2015).

[16] O. Zatsarinny and K. Bartschat, Nonperturbative Treatment of Ionization with Excitation of Helium by Electron Impact, Phys. Rev. Lett. **107**, 023203 (2011).

[17] X. Ren, T. Pflüger, S. Xu, J. Colgan, M. S. Pindzola, A. Senftleben, J. Ullrich, and A. Dorn, Strong Molecular Alignment Dependence of H_2 Electron Impact Ionization Dynamics, Phys. Rev. Lett. **109**, 123202 (2012).

[18] T. Pflüger, O. Zatsarinny, K. Bartschat, A. Senftleben, X. Ren, J. Ullrich, and A. Dorn, Electron-Impact Ionization of Neon at Low Projectile Energy: An Internormalized Experiment and Theory for a Complex Target, Phys. Rev. Lett. **110**, 153202 (2013).

[19] X. Ren, S. Amami, O. Zatsarinny, T. Pflüger, M. Weyland, W. Y. Baek, H. Rabus, K. Bartschat, D. Madison, and A. Dorn, Kinematically complete study of low-energy electron-impact ionization of neon: Internormalized cross sections in three-dimensional kinematics, Phys. Rev. A **91**, 032707 (2015).

[20] D. H. Madison and O. Al-Hagan, The distorted-wave Born approach for calculating electron-impact ionization of molecules, J. At. Mol. Opt. Phys. **2010**, 367180 (2010).

[21] C. M. Granados-Castro and L. U. Ancarani, Electron impact ionization of the outer valence orbital $1t_2$ of CH_4, Eur. Phys. J. D **71**, 65 (2017).

[22] K. L. Nixon, A. J. Murray, O. Al-Hagan, D. H. Madison, and C. Ning, Low-energy symmetric coplanar and symmetric noncoplanar (e,2e) studies from the $3a_1$ state of H_2O, J. Phys. B: At. Mol. Opt. Phys. **43**, 035201 (2010).

[23] C.-Y. Lin, C. W. McCurdy, and T. N. Rescigno, Complex Kohn approach to molecular ionization by high-energy electrons: Application to H_2O, Phys. Rev. A **89**, 012703 (2014).

[24] E. Ali, H. S. Chakraborty, and D. H. Madison, Improved theoretical calculations for electron-impact ionization of DNA analogue molecules, J. Chem. Phys. **152**, 124303 (2020).

[25] D. Jones, J. Builth-Williams, S. Bellm, L. Chiari, H. Chaluvadi, D. Madison, C. Ning, B. Lohmann, O. Ingólfsson, and M. Brunger, Dynamical (e,2e) investigations of tetrahydrofuran and tetrahydrofurfuryl alcohol as DNA analogues, Chem. Phys. Lett. **572**, 32 (2013).

[26] X. Ren, S. Amami, K. Hossen, E. Ali, C. G. Ning, J. Colgan, D. Madison, and A. Dorn, Electron-impact ionization of H_2O at low projectile energy: Internormalized triple-differential cross sections in three-dimensional kinematics, Phys. Rev. A **95**, 022701 (2017).

[27] E. Acebal and S. Otranto, Continuum-distorted-wave eikonal-initial-state description of the electron-impact ionization of H_2O at low impact energies, Phys. Rev. A **98**, 012703 (2018).

[28] M. Gong, X. Li, S. B. Zhang, S. Niu, X. Ren, E. Wang, A. Dorn, and X. Chen, Multicenter three-distorted-wave approach to three-dimensional images for electron-impact-ionization dynamics of molecules: Overall agreement with experiment, Phys. Rev. A **98**, 042710 (2018).

[29] L. S. Cederbaum, J. Zobeley, and F. Tarantelli, Giant Intermolecular Decay and Fragmentation of Clusters, Phys. Rev. Lett. **79**, 4778 (1997).

[30] E. Wang, X. Ren, and A. Dorn, Role of the Environment in Quenching the Production of H_3^+ from Dicationic Clusters of Methanol, Phys. Rev. Lett. **126**, 103402 (2021).

[31] X. Ren, J. Zhou, E. Wang, T. Yang, Z. Xu, N. Sisourat, T. Pfeifer, and A. Dorn, Ultrafast energy transfer between π-stacked aromatic rings upon inner-valence ionization, Nat. Chem. **14**, 232 (2022).

[32] T. Pflüger, A. Senftleben, X. Ren, A. Dorn, and J. Ullrich, Observation of Multiple Scattering in $(e, 2e)$ Experiments on Small Argon Clusters, Phys. Rev. Lett. **107**, 223201 (2011).

[33] J. Zhou, X. Yu, S. Luo, X. Xue, S. Jia, X. Zhang, Y. Zhao, X. Hao, L. He, C. Wang, D. Ding, and X. Ren, Triple ionization and fragmentation of benzene trimers following ultrafast intermolecular coulombic decay, Nat. Commun. **13**, 5335 (2022).

[34] F. Blanco and G. García, Electron interactions with Ar clusters and liquid Ar, J. Phys.: Conf. Ser. **438**, 012012 (2013).

[35] X. Ren, T. Pflüger, M. Weyland, W. Y. Baek, H. Rabus, J. Ullrich, and A. Dorn, An (e, 2e + ion) study of low-energy electron-impact ionization and fragmentation of tetrahydrofuran with high mass and energy resolutions, J. Chem. Phys. **141**, 134314 (2014).

[36] C. R. Stia, O. Fojon, P. F. Weck, J. Hanssen, and R. D. Rivarola, Interference effects in single ionization of molecular hydrogen by electron impact, J. Phys. B: At. Mol. Opt. Phys. **36**, L257 (2003).

[37] D. S. Milne-Brownlie, M. Foster, J. Gao, B. Lohmann, and D. H. Madison, Young-Type Interference in $(e, 2e)$ Ionization of H_2, Phys. Rev. Lett. **96**, 233201 (2006).

[38] X. Li, X. Ren, K. Hossen, E. Wang, X. Chen, and A. Dorn, Two-center interference in electron-impact ionization of molecular hydrogen, Phys. Rev. A **97**, 022706 (2018).

[39] M. Kunitski, N. Eicke, P. Huber, J. Köhler, S. Zeller, J. Voigtsberger, N. Schlott, K. Henrichs, H. Sann, F. Trinter, L. P. H. Schmidt, A. Kalinin, M. S. Schöffler, T. Jahnke, M. Lein, and R. Dörner, Double-slit photoelectron interference in strong-field ionization of the neon dimer, Nat. Commun. **10**, 1 (2019).

[40] H. Sann, C. Schober, A. Mhamdi, F. Trinter, C. Müller, S. K. Semenov, M. Stener, M. Waitz, T. Bauer, R. Wallauer, C. Goihl, J. Titze, F. Afaneh, L. P. H. Schmidt, M. Kunitski, H. Schmidt-Böcking, P. V. Demekhin, N. A. Cherepkov, M. S. Schöffler, T. Jahnke *et al.*, Delocalization of a Vacancy across Two Neon Atoms Bound by the van der Waals Force, Phys. Rev. Lett. **117**, 263001 (2016).

[41] O. F. Hagena, Nucleation and growth of clusters in expanding nozzle flows, Surf. Sci. **106**, 101 (1981).

[42] S. J. Ward and J. H. Macek, Wave functions for continuum states of charged fragments, Phys. Rev. A **49**, 1049 (1994).

[43] O. Zatsarinny, BSR: B-spline atomic R-matrix codes, Comput. Phys. Commun. **174**, 273 (2006).

[44] O. Zatsarinny and K. Bartschat, The B-spline R-matrix method for atomic processes: Application to atomic structure, electron collisions and photoionization, J. Phys. B: At. Mol. Opt. Phys. **46**, 112001 (2013).

[45] M. Gong, Y. Zhang, X. Li, S. B. Zhang, X. Shan, and X. Chen, Distorted-wave description of electron momentum spectroscopy for molecules: A demonstration for molecular oxygen, Phys. Rev. A **105**, 042805 (2022).

[46] X. Ren, E. Jabbour Al Maalouf, A. Dorn, and S. Denifl, Direct evidence of two interatomic relaxation mechanisms in argon dimers ionized by electron impact, Nat. Commun. **7**, 11093 (2016).

[47] X. Ren, T. Miteva, P. Kolorenč, K. Gokhberg, A. I. Kuleff, L. S. Cederbaum, and A. Dorn, Observation of fast and slow interatomic coulombic decay in argon dimers induced by electron-impact ionization, Phys. Rev. A **96**, 032715 (2017).

[48] M. J. Brunger, I. E. McCarthy, and E. Weigold, High-resolution electron-momentum spectroscopy of argon: Validation of technique and approximations, Phys. Rev. A **59**, 1245 (1999).

[49] M. Foster, J. L. Peacher, M. Schulz, D. H. Madison, Z. Chen, and H. R. J. Walters, Unexpected Higher-Order Effects in Charged Particle Impact Ionization at High Energies, Phys. Rev. Lett. **97**, 093202 (2006).

[50] X. Ren, A. Senftleben, T. Pflüger, A. Dorn, K. Bartschat, and J. Ullrich, Signatures of projectile–nucleus

scattering in three-dimensional (e,2e) cross sections for argon, J. Phys. B: At. Mol. Opt. Phys. **43**, 035202 (2010).

[51] X. Ren, A. Senftleben, T. Pflüger, A. Dorn, K. Bartschat, and J. Ullrich, Benchmark experiment for electron-impact ionization of argon: Absolute triple-differential cross sections via three-dimensional electron emission images, Phys. Rev. A **83**, 052714 (2011).

[52] X. Ren, T. Pflüger, J. Ullrich, O. Zatsarinny, K. Bartschat, D. H. Madison, and A. Dorn, Low-energy electron-impact ionization of argon: Three-dimensional cross section, Phys. Rev. A **85**, 032702 (2012).

[53] X. Ren, T. Pflüger, J. Ullrich, O. Zatsarinny, K. Bartschat, D. H. Madison, and A. Dorn, Erratum: Low-energy electron-impact ionization of argon: Three-dimensional cross section, Phys. Rev. A **92**, 019901(E) (2015).

[54] X. Ren, A. Senftleben, T. Pflüger, J. Ullrich, K. Bartschat, and A. Dorn, Erratum: Benchmark experiment for electron-impact ionization of argon: Absolute triple-differential cross sections via three-dimensional electron emission images, Phys. Rev. A **89**, 029904(E) (2014).

[55] W. R. Wadt, The electronic states of Ar_2^+, Kr_2^+, Xe_2^+. I. Potential curves with and without spin-orbit coupling, J. Chem. Phys. **68**, 402 (1978).

[56] W. J. Stevens, M. Gardner, A. Karo, and P. Julienne, Theoretical determination of bound-free absorption cross sections in Ar_2^+, J. Chem. Phys. **67**, 2860 (1977).

[57] B. J. Whitaker, C. A. Woodward, P. J. Knowles, and A. J. Stace, On the origin of metastable decay in Ar_2^+, J. Chem. Phys. **93**, 376 (1990).

[58] M. J. Frisch, G. W. Trucks, H. B. Schlegel, G. E. Scuseria, M. A. Robb, J. R. Cheeseman, G. Scalmani, V. Barone, G. A. Petersson, H. Nakatsuji, X. Li, M. Caricato, A. V. Marenich, J. Bloino, B. G. Janesko, R. Gomperts, B. Mennucci, H. P. Hratchian, J. V. Ortiz, A. F. Izmaylov *et al.*, *Gaussian 16 Revision A.03* (Gaussian, Wallingford, CT, 2016).

[59] N. Watanabe, X. J. Chen, and M. Takahashi, Interference Effects on (e, 2e) Electron Momentum Profiles of CF_4, Phys. Rev. Lett. **108**, 173201 (2012).

[60] E. Wang, E. Ali, X. Li, X. Ren, X. Chen, D. Madison, and A. Dorn, Molecular-frame (e, 2e) ionization dynamics of H2 at high impact-energy, Eur. Phys. J. D **74**, 105 (2020).